Experimental Design for Voltage Driven Tracer Incorporation and Diffusion Studies on Oxide Thin Film Electrodes

Tobias M. Huber,[a,b,c,d,e,=,*] Edvinas Navickas,[e,=] Kazunari Sasaki,[a,b,f,g,*] Bilge Yildiz,[d,*] Harry Tuller,[b,c] Gernot Friedbacher,[e] Herbert Hutter,[e] and Juergen Fleig[e,*,z]

[a]*Next-Generation Fuel Cell Research Center (NEXT-FC), Kyushu University, Nishi-ku, Fukuoka 819-0395, Japan*
[b]*International Institute for Carbon-Neutral Energy Research (WPI-I2CNER), Kyushu University, Nishi-ku, Fukuoka 819-0395, Japan*
[c]*Department of Materials Science and Engineering, Massachusetts Institute of Technology, Cambridge, Massachusetts 02139, USA*
[d]*Laboratory for Electrochemical Interfaces, Department of Nuclear Science and Engineering, Massachusetts Institute of Technology, Cambridge, Massachusetts 02139, USA*
[e]*Institute of Chemical Technologies and Analytics, Vienna University of Technology, Vienna A-1060, Austria*
[f]*Department of Mechanical Engineering, Faculty of Engineering, Kyushu University, Nishi-ku, Fukuoka 819-0395, Japan*
[g]*International Research Center for Hydrogen Energy, Kyushu University, Nishi-ku, Fukuoka 819-0395, Japan*

The effect of an applied overpotential on oxygen isotope incorporation and diffusion in oxide thin film electrodes is investigated by a novel experimental approach. A special electrode geometry leads to in-plane electron flow, perpendicular oxide ion flow and a well-defined laterally varying driving force. This design allows one to obtain a series of tracer depth profiles induced by a range of overpotentials on one and the same thin film. The approach was applied to $La_{0.8}Sr_{0.2}MnO_3$ (LSM) thin films deposited by pulsed laser deposition (PLD) on yttria stabilized zirconia (YSZ) single crystals. Tracer depth profiles were measured by secondary ion mass spectrometry (SIMS). These depth profiles include examples of pronounced apparent uphill diffusion that can be explained by considering an interplay of polarization-induced changes in stoichiometry within the LSM grains combined with fast oxygen transport along the grain boundaries.
 [DOI: 10.1149/2.0711707jes]

Manuscript submitted March 2, 2017; revised manuscript received May 3, 2017. Published May 16, 2017.

Solid oxide fuel cells (SOFCs) offer some of the highest chemical to electrical energy conversion efficiencies, exhibit high fuel flexibility – i.e. able to operate with hydrocarbon fuels in addition to hydrogen and show a high tolerance to typical catalyst poisons, all associated with their elevated operating temperatures, typically above 600–700°C. Cathodes of SOFCs are generally based on perovskite-type oxides such as $La_{1-x}Sr_xMnO_{3-\delta}$,[1–4] $La_{1-x}Sr_xFeO_{3-\delta}$[5–7] and $La_{1-x}Sr_xCoO_{3-\delta}$.[8–11] The electrocatalytic properties of these electrode materials depend not only on their cation composition and their detailed surface chemistry, but can also be strongly impacted by the chemical potential of oxygen and, in turn, by applied overpotentials. Depending on the ionic conductivity of these electrode materials, oxygen reduction may take place via the so-called bulk path (two phase boundary), with oxygen reduction at the oxide surface followed by oxygen ion transport through the electrode to the electrolyte. An active and fast bulk path, together with an optimal microstructure, enables low polarization resistances and thus superior electrochemical performance of SOFC electrodes. For an effective electrode design, it is thus important to know the kinetic parameters associated with both surface and bulk related electrochemical processes associated with oxygen reduction, incorporation and diffusion via the bulk path, including their dependence on current load. However, it is not always simple to deconvolute these contributions to overall voltage dependent polarization resistances associated with SOFC electrodes.

Several approaches are commonly used to attempt such deconvolutions. One approach employs impedance spectroscopy and the modelling of the spectra in terms of equivalent circuits.[12] Another powerful technique is based on oxygen tracer incorporation and the subsequent analysis of the resulting depth profiles. This yields surface exchange parameters and diffusion coefficients[13,14] and may also indicate reaction pathways, particularly when under bias.[15–18] In a recent study, we examined bias-voltage-induced tracer incorporation into lanthanum strontium manganite (LSM) thin film electrodes. This lead to surprising tracer profiles with apparent uphill diffusion at higher overpotentials.[19] However, given the nature of oxygen exchange experiments, in contrast to bias dependent impedance measurements, a systematic study of the bias dependent tracer incorporation requires many different samples, one for each bias voltage.

In this contribution, we suggest a novel approach that markedly simplifies bias dependent tracer incorporation measurements. A specified electrode geometry allows one to spatially vary the overpotential for oxygen reduction along a mixed conducting electrode in a well defined manner. This then enables us to obtain tracer incorporation data as a function of electrochemical driving forces on one and the same thin film electrode. The method is applied to LSM thin films deposited onto yttria stabilized zirconia (YSZ) solid electrolytes with a variety of LSM microstructures with the results analyzed and the opportunities and limitations associated with this approach discussed.

Experimental

Two types of LSM thin films, with two different microstructures and thicknesses, were prepared from a $La_{0.8}Sr_{0.2}MnO_3$ target by pulsed laser deposition (PLD) at 600°C (LSM_{600}) and 800°C (LSM_{800}) respectively. Both layers were deposited on yttria stabilized zirconia (YSZ, 9.5 mol% Y_2O, CrysTec GmbH, Germany) single crystal substrates. Deposition was performed at $4 \cdot 10^{-2}$ mbar oxygen partial pressure using a KrF excimer laser with a wavelength of 248 nm and a pulse frequency of 5 Hz. The laser beam energy was set to 400 mJ per pulse and a target-substrate distance of 6 cm was used. For the given deposition parameters, columnar structured LSM layers resulted.[14] Topographical images of the LSM thin films obtained by atomic force microscopy are shown in Figs. 1a and 1b. The LSM thin film deposited at 600°C shows a surface topography with well-defined and narrow grains, with a grain diameter of about 30 nm estimated from a line scan. As shown by transmission electron microscopy (TEM) in Refs. 14,19, LSM layers deposited at 600°C had grain diameters of ca. 30 nm. The LSM_{800} sample was post-annealed at 940°C to induce further grain growth, resulting in grains nearly twice as large as those of LSM_{600}. The surface coarsened LSM_{800} exhibited a much higher

=These authors contributed equally to this work.
*Electrochemical Society Member.
zE-mail: j.fleig@tuwien.ac.at

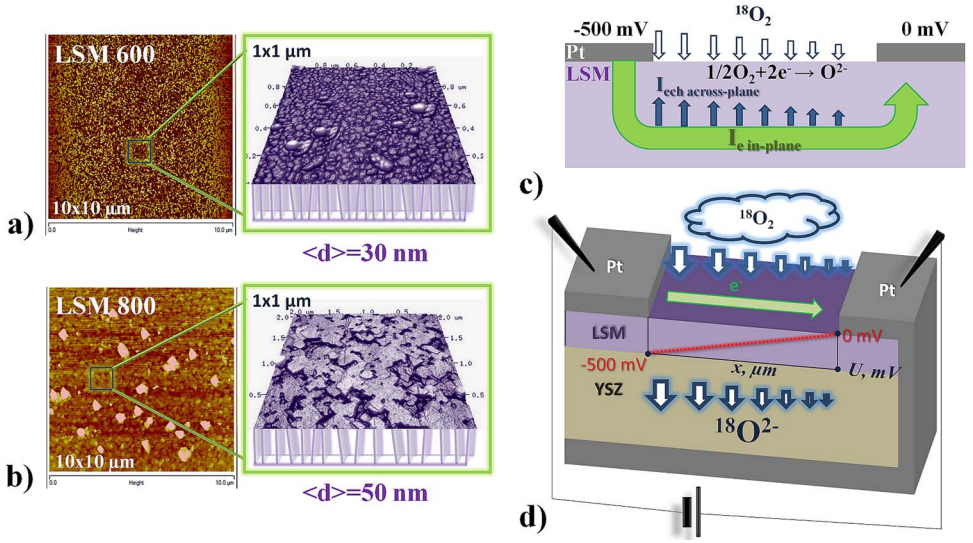

Figure 1. The AFM images of as deposited LSM_{600} (a) and LSM_{800} (b) thin films show different surface topography due to different thin film microstructure. c) The electron source is the negative Pt stripe with two electron sinks: Either electrons flow to the positive Pt stripe electrode ($I_{e,in\text{-}plane}$) or they are consumed in the oxygen incorporation reaction ($I_{e,in\text{-}plane}$). Due to high oxygen incorporation and diffusion resistance most of the current flows to the electron sink at the 0 V Pt stripe; only very little electronic current is transferred to ionic current at the surface. d) Sketch of the sample design with two Pt stripe electrodes on top of LSM, one connected to the bottom counter electrode. Also the local overpotential and the different types of current (e^-, O^{2-}) are sketched.

average surface roughness (Fig. 1b) hindering determination of the exact grain width from AFM images.

After PLD deposition two parallel platinum electrodes were prepared on top of the LSM layers by UV lithography and subsequent DC magnetron sputtering (MED 020 Coating System, BAL-TEC, Germany). The stripe distance was ca. 7.5 mm, with stripe widths of 1 mm. Porous Pt counter electrodes were applied with the aid of Pt paste on the back side of each YSZ single crystal and connected to one of the Pt stripe electrodes on top. A sketch of the sample geometry is given in Fig. 1d. Electrical measurements were performed by applying a DC voltage between the two Pt electrodes using a POT/GAL 30 V 2A test interface together with an Alpha- A High Resolution Dielectric Analyzer (both Novocontrol, Germany) in DC mode (software WINCHEM and WINDETA Novocontrol, Germany).

Additionally van der Pauw measurements were performed on LSM films deposited on YSZ or sapphire substrates with the films contacted at their edges by Pt electrodes. This allowed determination of the temperature dependent in-plane electronic conductivity. Electrochemical polarization resistances were estimated from DC current measurements on polarized microelectrodes (490 × 490 μm^2), prepared from LSM_{600} thin films on YSZ by PLD.[19] In this case a porous Pt counter electrode applied to the back of the YSZ substrate was used.

Oxygen tracer incorporation into the sample with Pt stripes on the LSM film took place in a symmetrically heated quartz oxygen tracer exchange chamber (Huber-Scientific, Austria) in a tube furnace. The symmetrical heating ensures a homogeneous temperature distribution within the sample. The experiments were performed at 603°C for LSM_{600} and at 642°C for LSM_{800}. $^{18}O_2$ oxygen tracer gas (200 hPa, 97.1%, Campro Scientific, Germany) was filled into the chamber and within a few seconds a cathodic bias of –500 mV for LSM_{600} and −600 mV for LSM_{800} was applied for 10 minutes between the two platinum stripes. The DC current was monitored during the isotope exchange experiments. After 10 minutes, the voltage was switched off, and the sample was quenched to room temperature. A pre-annealing step of the thin films prior to the tracer gas exposure was performed in lab air for 60 minutes to ensure equilibration of the specimen with the atmosphere. Please note that evacuation prior to tracer gas filling, given its lower effective pO_2, partly compensates this equilibration step and at least for the very near surface region places the LSM thin films in a not completely defined defect chemical state prior to tracer and voltage exposure. Hence, the driving force for tracer incorporation is not only the tracer concentration difference and the applied local overpotential, but also some oxygen chemical potential difference. A further equilibration step in the tracer gas prior to voltage load, however, would be even more problematic, since it would lead to a tracer profile determined by a certain time span without voltage and the time upon applied voltage. Fortunately, in the case of LSM the errors due to chemical potential differences between sample and gas at the beginning of the experiment are considered negligible, due to the very small oxygen vacancy concentration present in unpolarized LSM.[20] More detailed information on this topic, with oxygen isotope exchange experiments on Sr-doped $LaCoO_3$ thin layers, is given in Ref. 21.

The resulting ^{18}O depth profiles were subsequently investigated by time-of-flight secondary ion mass spectrometry (ToF-SIMS 5, ION-TOF GmbH, Germany). Measurements were done in the collimated burst alignment (CBA) mode with Bi^{3++} primary ions (25 keV). Negative secondary ions were analyzed in the area of 70 × 70 μm^2. The sputtering of LSM was performed with Cs^+ ions (2 keV, $I_{sputter\_current}$ = 115 nA) with a defined sputter crater of 350 × 350 μm^2. Surface charging was compensated with an electron flood gun. The isotope exchange depth profiles (tracer fraction $f(^{18}O)$) were obtained by normalizing integrated intensities I of ^{18}O and ^{16}O in the mass spectra according to

$$f(^{18}O) = \frac{I(^{18}O)}{I(^{16}O) + I(^{18}O)} \quad [1]$$

The sputtering rate (0.4 nm/s) of LSM thin films was determined from the depth of the sputtered crater for a given sputtering time. This depth was measured by digital holographic microscopy (DHM, Lyncee Tec, Switzerland) and revealed layer thicknesses of 190 nm and 770 nm for LSM_{600} and LSM_{800}, respectively.

Results and Discussion

Working principle of the novel electrode design for voltage driven tracer incorporation.—The "unusual" electrode geometry used here leads to a special charge carrier flow in the sample with a mixed ion-electron conducting top electrode. Since YSZ is blocking for electrons, electrons only flow within the mixed ionic and electronic conductor (MIEC) used as a thin film electrode. The electron source is the negative Pt stripe, while two electron sinks are present: Either electrons

flow to the positive Pt stripe electrode or they are consumed in the oxygen incorporation reaction ($1/2O_2 + 2e^- \rightarrow O^{2-}$) as shown in Fig. 1c. Let us assume that the sum of the oxygen incorporation resistance into the MIEC and the ion transport across the MIEC are much higher than the resistance of in-plane electron transport. Then most of the current flows to the electron sink at the 0 V Pt stripe ($I_{e,in\text{-}plane}$); only very little electronic current is transferred to ionic current at the surface ($I_{ech,across\text{-}plane}$). If this condition of $I_{e,in\text{-}plane} >> I_{ech,across\text{-}plane}$ is not fulfilled, the MIEC layer thickness and the distance between the Pt stripes may be modified. Both geometrical parameters affect the two currents in opposite ways: A larger Pt stripe distance, for example, increases $I_{ech,across\text{-}plane}$ but decreases $I_{e,in\text{-}plane}$. Moreover, we assume that the conductivity of the MIEC is not affected by the local electrochemical potential of electrons, but is constant along the entire film. In such a situation, the resulting electrochemical potential distribution of electrons in the MIEC can be approximated by a linear voltage drop in a homogeneous conductor, see sketch of the linearly changing voltage U in Fig. 1d.

The current due to oxygen incorporation into the MIEC thin film electrode and subsequent ion transport across the YSZ layer is thus small compared to the measured current. However, this does not imply that the corresponding driving force is small as well. Rather, this driving force can be as large as the entire applied voltage (close to the negative Pt stripe). It decays linearly toward the positively polarized Pt stripe and hence a well-defined (but varying) voltage can be attributed to each position in the MIEC electrode. Provided the electrochemical resistances of the YSZ electrolyte and the counter electrode are much smaller than that of oxygen incorporation and transport in the MIEC, the applied local voltage is nearly equal to the overpotential of the MIEC electrode at the given position. The electrochemical processes are also sketched in Fig. 1d: Close to the left Pt stripe much more oxygen is reduced and transported to the counter electrode than close to the Pt stripe at 0 V. This is the novelty of our cell design: an electrode with laterally varying but still with a well-defined overpotential. In conventional DC or impedance measurements such a spatially varying overpotential would strongly complicate the analysis of any measured current and should be avoided. In a tracer experiment with spatially resolved detection of tracer profiles, however, this variation allows us to probe the effect of different overpotentials within one and the same MIEC thin film and from a single tracer incorporation experiment. Close to the left Pt stripe and thus for high cathodic driving force the tracer incorporation is strongly affected by the voltage while close to the other Pt stripe mainly thermally driven oxygen tracer exchange takes place.

Applicability of the method to LSM.—The prerequisite for straightforward application of the method to our LSM thin films is the need for a much larger electronic in-plane current compared to the across-plane ionic current due to oxygen reduction at the LSM surface. In our specific case this was confirmed by pursuing the following experiments. First, the electronic conductivity of the LSM films was measured by the van der Pauw technique. The resulting temperature dependent conductivities are shown in Fig. 2a. Obviously, the LSM_{600} film with small grains exhibits a smaller conductivity than the film with larger grains. The LSM_{800} electronic conductivity nearly reaches the literature value of bulk LSM.[22,23] The grain boundaries are believed to lower the conductivity of LSM_{600}; a detailed discussion of this will be given in a forthcoming paper. From these conductivity values we can predict the expected electronic in-plane current in our polarization experiments; $I_{e,in\text{-}plane} = 0.59$ mA (LSM_{600}) and $I_{e,in\text{-}plane} = 6.71$ mA (LSM_{800}) result from the data in Fig. 2a for our electrode geometry. The much larger value for the LSM_{800} film is primarily due to its larger thickness ($t(LSM_{800}) = 770$ nm and $t(LSM_{600}) = 190$ nm). The measured current versus time curves after switching on the voltage is shown in Figs. 2b and 2c. The sharp decay for short times can be assigned to capacitive charging. The steady state currents ($I_{e,in\text{-}plane} = 1.30$ mA (LSM_{600}) and $I_{e,in\text{-}plane} = 6.07$ mA (LSM_{800})) are in good agreement with the predicted currents and indicate that in our experiment, the current is indeed largely the in-plane electron current between the two Pt stripes. The very small increase in the current on a longer time scale, visible for the LSM_{800} sample with larger grains, possibly reflects the change of the (small) electrochemical part of the current, i.e. $I_{ech,across\text{-}plane}$, due to stoichiometry polarization of the LSM film.

For the given electrode geometry the electrochemical polarization resistance of LSM due to oxygen reduction cannot be measured electrically. Hence, an estimate of this polarization resistance was obtained from experiments with LSM_{600} microelectrodes on YSZ measured against a porous Pt counter electrode. Figs. 2d and 2e display current versus time curves of such electrodes for different temperatures and voltage values. The interpretation of the detailed time dependence is beyond the scope of this paper. Essential for our discussion is the steady state current found after some time, indicating resistances larger than $1.5 \cdot 10^5\ \Omega \cdot cm^2$ at 608°C even for the highest polarization of −450 mV. This can be transferred to an upper estimate of the ionic across-plane current in our tracer exchange experiments. For the values in Fig. 2e (−450 mV) we get $I_{ech,across\text{-}plane} = 7$ nA and thus a value that is much smaller than $I_{in\text{-}plane}$. Hence, our prerequisite assumption, in terms of predominant electron current between the Pt stripes, is fulfilled.

Still, we have to be aware of the fact that parts of the LSM film are at a low oxygen chemical potential due to the applied cathodic voltage. Hence, also the lateral homogeneity of the electronic current should be checked. According to existing defect chemical models of LSM, the voltage or partial pressure range considered here should only lead to minor changes in the electronic charge carrier concentration and thus a significant drop of the electronic conductivity along the LSM film is not expected.[20]

Measured tracer profiles.—Isotope depth profiles were measured at different positions of the LSM film after exposure to a bias voltage in an $^{18}O_2$ tracer atmosphere. Different distances from the negatively polarized Pt stripe can be assigned to different local overpotentials. The optical microscopy images of the LSM films with the SIMS sputter craters are shown in Figs. 3a and 3d, together with local overpotentials calculated from the model assumption of a linear voltage decay between the electrodes. The corresponding tracer depth profiles at different locations of the LSM films are shown in Figs. 3b and 3e on a linear scale and in Figs. 3c and 3f on a logarithmic scale.

The SIMS measurements close to the zero volt stripe electrode lead to tracer profiles that consist of two parts, a steep ^{18}O decrease close to the surface followed by a shallow ^{18}O decay (Figs. 3b, 3c at −0.033 V). In accordance with Refs. 14,19 this indicates two parallel diffusion processes: The first profile part is dominated by diffusion via the bulk of the LSM grains, while the second part comes from diffusion along grain boundaries and continuous tracer "leakage" from the grain boundaries into the grains. Essentially, this is similar to a situation known as Harrison's Type B regime.[24] When moving closer to the negative Pt stripe, the tracer depth profiles change their shape. In particular for LSM_{600}, the tracer fraction decrease near to the surface is followed by an increased isotope concentration at deeper depths (Figs. 3b and 3c at voltages larger than about 200 mV). A maximum is reached at some depth and the tracer fraction again decreases toward the LSM/YSZ interface. Similar apparent uphill diffusion profiles were already reported in our previous study on LSM microelectrodes.[19] They result from a combination of fast oxygen diffusion along grain boundaries and depth dependent bias activated "leakage" into the bulk, see the detailed discussion below. It should be emphasized that only the given electrode geometry with well-defined lateral variation of the overpotential enabled us to collect this large amount of information from a single tracer experiment.

Measurements on the thicker LSM_{800} thin film with larger grains also show a dependence of the shape of the diffusion profile on the driving force, but with a reduced apparent uphill diffusion and then only found for the highest polarization values and only very close to the surface. The modified shapes compared to the non-biased situation can again be explained by considering the combination of fast grain

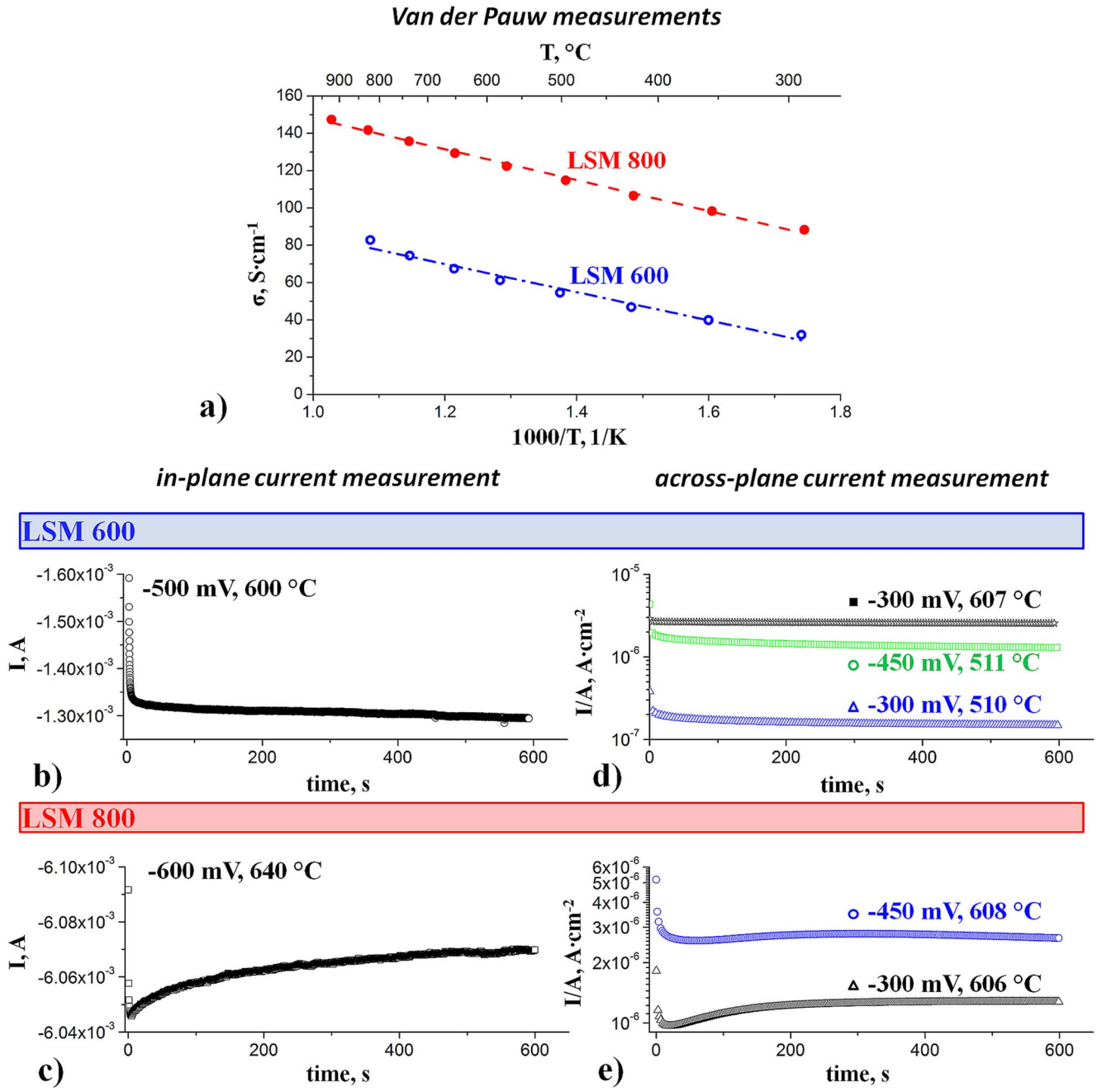

Figure 2. a) Plot showing the electronic in-plane conductivity of LSM thin films with different microstructures deposited at 600°C and 800°C. The in-plane current over time was measured during polarization experiments in $^{18}O_2$ atmosphere on LSM_{600} (600°C, −500 mV) (b) and on LSM_{800}: (640°C, −600 mV) (c)). Across-plane current measurements on LSM_{600} (d) and LSM_{800} (e) microelectrodes at different temperatures and voltages.

boundary diffusion and stoichiometry polarization of the bulk; see below. The larger grains obviously reduce the impact of grain boundary diffusion on the inbound flux of ^{18}O and moreover, a higher fraction of the driving force drops at the LSM surface due to surface degradation (keeping in mind that the LSM_{800} sample was post-annealed). This results in a less pronounced stoichiometry polarization of the grain bulk.

Interpretation of the measured tracer profiles.—In order to analyze the bias modified profiles, including the uphill-type isotope profiles in LSM_{600}, the effect of bias voltage on oxygen incorporation and diffusion in LSM has to be discussed in more detail. Firstly, two parallel diffusion pathways exist for oxygen ions in columnar LSM: oxygen diffusion through the LSM grain and diffusion along the grain boundaries. It was already shown in Refs. 13,14,19 that grain boundaries exhibit tracer diffusion coefficients that are several orders of magnitude larger than in the bulk. Still, for the diffusion times employed here, the concentration of tracer ions decays strongly along a grain boundary, i.e. from the surface to the LSM/YSZ interface, see width of the blue arrows in Fig. 4a. Secondly, application of a voltage to LSM/YSZ causes stoichiometry polarization of the LSM layer since the YSZ substrate is electronically blocking. This leads to a depth-dependent chemical potential μ_O which drastically changes the oxygen vacancy concentration as shown in Fig. 4a. Hence, the concentration of oxygen vacancies in the bulk becomes much higher close to the LSM/YSZ interface than at the LSM surface and the tracer diffusion coefficient in the LSM bulk is modified accordingly: tracer diffusion in LSM grains is rather slow close to the surface but

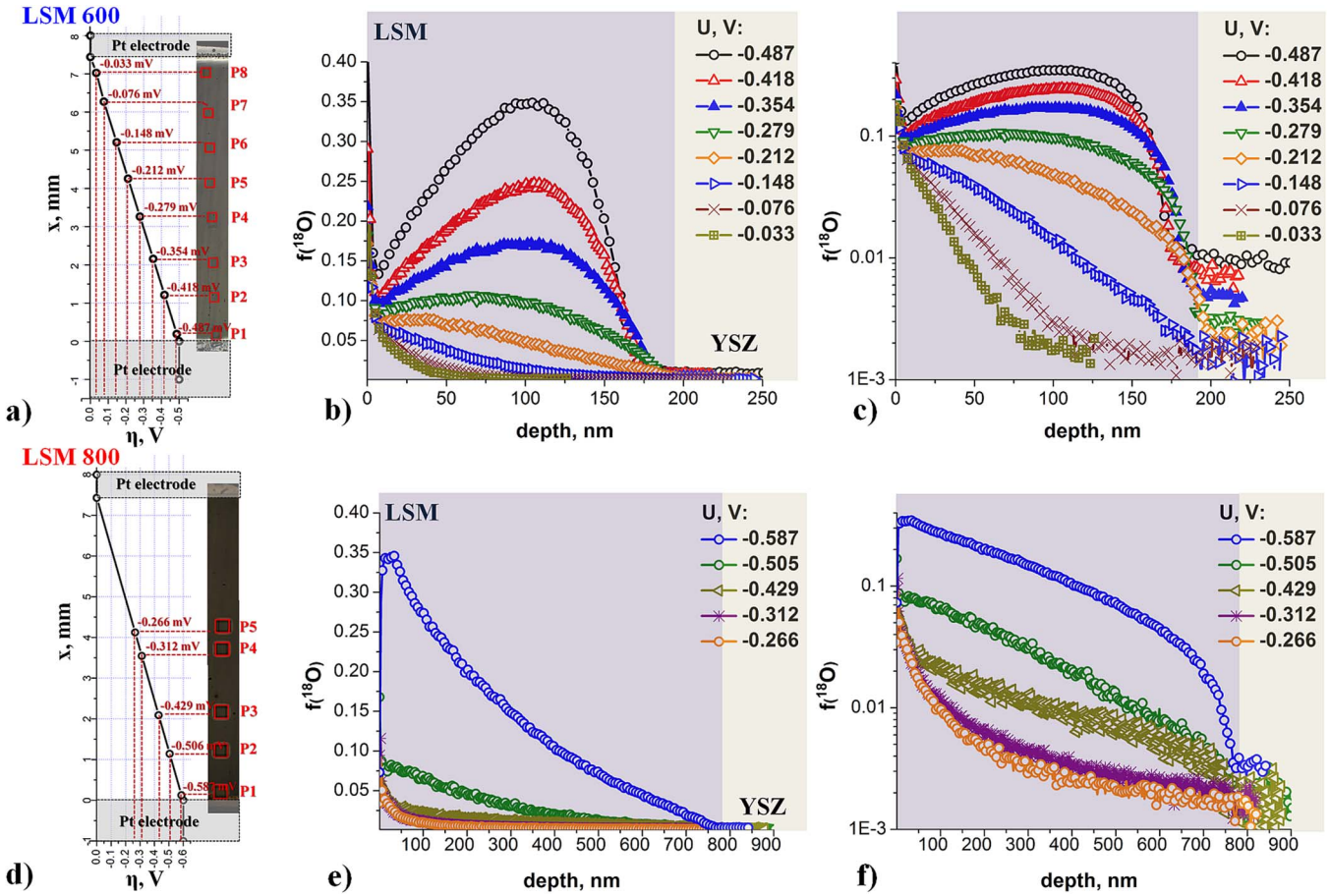

Figure 3. The overpotential related oxygen isotope depth profiles were measured at different positions which refers to different local biases (a and d). The obtained SIMS isotope depth profiles on LSM_{600} (b) have pronounced uphill diffusion shape at higher overpotentials. In the logarithmic plot the change of the second diffusion part is well visible: close to the 0 V Pt stripe (−0.033 V) the diffusion profile looks like that known from columnar LSM thin films, while SIMS measurements close to the negative Pt stripe have well pronounced uphill diffusion profile shape. The uphill diffusion part becomes less pronounced in LSM_{800} (e and f) due to the wider grains and different surface properties.

becomes faster toward the LSM/YSZ interface (shown by red arrows in Fig. 4a).

The combination of these two aspects can explain the occurrence of the "tracer hill" in the center of the sample. As sketched in Fig. 4b the combination of still reasonably high tracer concentration in the grain boundary and already substantially increased tracer diffusion coefficient in the grain leads to the strongest flux ("leakage") of tracer ions from the grain boundary into the grain and thus to the "hill" measured in the tracer profile. Depending on the local overpotential of the film, the stoichiometry polarization in the grain changes and the accelerating effect of the stoichiometry polarization in terms of high tracer diffusion coefficient due to high oxygen vacancy concentration becomes less pronounced for smaller overpotentials. Therefore, the tracer hill is most pronounced for the highest overpotential. Please note that the depth profiles obtained by SIMS always represent an integration over the entire investigated area

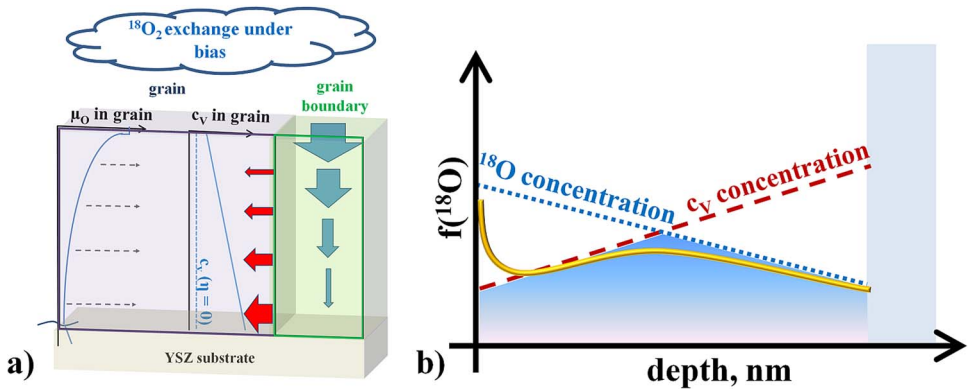

Figure 4. a) The oxygen chemical potential and vacancy concentration redistribution under applied bias leads a higher oxygen vacancy concentration at the YSZ/LSM interface. In the fast diffusing grain boundaries, more isotope is available at the surface and less at the interface, which in combination with the oxygen vacancy redistribution under bias, leads to a maximum concentration in the middle of the LSM layer (b).

(70 μm × 70 μm) and thus includes regions with slightly varying overpotential (ca. ±5.6 mV variation within each measurement spot).

Conclusions

This study introduces a novel experimental design to facilitate voltage driven tracer exchange experiments on thin film electrodes. The design allows one to investigate multiple applied overpotentials on one and the same sample during a single tracer experiment. In comparison to microelectrode measurements, this geometry has a number of advantages: It becomes i) easier to establish the electrical contact, ii) faster compared to many individual tracer measurements, iii) possible to analyze the impact of every overpotential value (from 0 V to U_{max} applied) on oxygen diffusion and incorporation. The prerequisite of this method is an electrochemical polarization resistance that is much larger than the in-plane electronic resistance that may be insured by selecting an appropriate film thickness and current collector distance. This new experimental approach was applied to LSM thin films with two different microstructures. The isotope diffusion profiles under bias, at times show an unusual apparent uphill diffusion that can be explained by a combination of stoichiometry polarization and fast grain boundary diffusion in the LSM layer.

Acknowledgments

T. M. Huber, K. Sasaki, acknowledge financial support from the Progress-100 program at Kyushu University. E. Navickas and J. Fleig acknowledge support from Austrian Science Fund (FWF) (project: F4509-N16), H. L. Tuller and B. Yildiz acknowledge US-DOE Basic Energy Sciences, grant No. DE-SC0002633 for financial support of their contributions.

References

1. J. Fleig, *Annual Review of Materials Research*, **33**, 361 (2003).
2. D. S. Mebane, Y. Liu, and M. Liu, *Solid State Ionics*, **178**, 1950 (2008).
3. S. B. Adler, *Chemical Reviews*, **104**, 4791 (2004).
4. L. Yan, B. Kavaipatti, K. -C. Chang, H. You, and P. Salvador, *ECS Transactions*, **35**, 2063 (2011).
5. S. Kogler, A. Nenning, G. M. Rupp, A. K. Opitz, and J. Fleig, *Journal of The Electrochemical Society*, **162**, F317 (2015).
6. M. Kuhn, S. Hashimoto, K. Sato, K. Yashiro, and J. Mizusaki, *Solid State Ionics*, **195**, 7 (2011).
7. M. Mosleh, M. Søgaard, and P. V. Hendriksen, *Journal of The Electrochemical Society*, **156**, B441 (2009).
8. Y. Takeda, R. Kanno, M. Noda, Y. Tomida, and O. Yamamoto, *J. Electrochem. Soc.: Electrochem. Sci. Technol.*, **134**, 2656 (1987).
9. A. Egger, E. Bucher, M. Yang, and W. Sitte, *Solid State Ionics*, **225**, 55 (2012).
10. A. N. Petrov, O. F. Kononchuk, A. V. Andreev, V. A. Cherepanov, and P. Kofstad, *Solid State Ionics*, **80**, 189 (1995).
11. G. M. Rupp, H. Tellez, J. Druce, A. Limbeck, T. Ishihara, J. Kilner, and J. Fleig, *Journal of Materials Chemistry A*, **3**, 22759 (2015).
12. M. Kubicek, T. M. Huber, A. Welzl, A. Penn, G. M. Rupp, J. Bernardi, M. Stöger-Pollach, H. Hutter, and J. Fleig, *Solid State Ionics*, **256**, 38 (2014).
13. A. M. Saranya, D. Pla, A. Morata, A. Cavallaro, J. Canales-Vázquez, J. A. Kilner, M. Burriel, and A. Tarancón, *Advanced Energy Materials*, **5**, 1500377-n/a (2015).
14. E. Navickas, T. M. Huber, Y. Chen, W. Hetaba, G. Holzlechner, G. Rupp, M. Stoger-Pollach, G. Friedbacher, H. Hutter, B. Yildiz, and J. Fleig, *Physical Chemistry Chemical Physics*, **17**, 7659 (2015).
15. T. Horita, K. Yamaji, N. Sakai, M. Ishikawa, H. Yokokawa, T. Kawada, and M. Dokiya, *Electrochem. Solid State Lett.*, **1**, 4 (1998).
16. T. Horita, K. Yamaji, N. Sakai, H. Yokokawa, T. Kawada, and T. Kato, *Solid State Ionics*, **127**, 55 (2000).
17. T. Horita, K. Yamaji, N. Sakai, X. P. Xiong, T. Kato, H. Yokokawa, and T. Kawada, *J. Power Sources*, **106**, 224 (2002).
18. A. K. Opitz, M. Kubicek, S. Huber, T. Huber, G. Holzlechner, H. Hutter, and J. Fleig, *Journal of Materials Research*, **28**, 2085 (2013).
19. T. M. Huber, E. Navickas, G. Friedbacher, H. Hutter, and J. Fleig, *ChemElectroChem*, **2**, 1487 (2015).
20. F. W. Poulsen, *Solid State Ionics*, **129**, 145 (2000).
21. M. Kubicek, Z. Cai, W. Ma, B. Yildiz, H. Hutter, and J. Fleig, *ACS Nano*, **7**, 3276 (2013).
22. Y. Ji, J. A. Kilner, and M. F. Carolan, *Solid State Ionics*, **176**, 937 (2005).
23. J. Mizusaki, Y. Yonemura, H. Kamata, K. Ohyama, N. Mori, H. Takai, H. Tagawa, M. Dokiya, K. Naraya, T. Sasamoto, H. Inaba, and T. Hashimoto, *Solid State Ionics*, **132**, 167 (2000).
24. L. G. Harrison, *Transactions of the Faraday Society*, **57**, 1191 (1961).